E Wolfrum et al.

Impact of wall materials and seeding gases on the pedestal and on core plasma performance

Impact of wall materials and seeding gases on the pedestal and on core plasma performance

E. Wolfrum[1], M. Beurskens[2], M.G. Dunne[1], L. Frassinetti[3], X. Gao[4], C. Giroud[5], J. Hughes[6], T. Lunt[1], R. Maingi[7], T. Osborne[8], M. Reinke[9], H. Urano[10], the ASDEX Upgrade Team and the EUROfusion MST1 Team[*]

[1]*Max-Planck-Institute for Plasma Physics, D - 85748 Garching, Germany*
[2]*Max-Planck-Institute for Plasma Physics, D - 17491Greifswald, Germany*
[3]*Division of Fusion Plasma Physics, KTH Royal Institute of Technology, Stockholm SE*
[4]*Institute of Plasma Physics, Chinese Academy of Sciences, Hefei 230031, People's Republic of China*
[5]*EURATOM/CCFE Fusion Association, Culham Science Centre, Abingdon, Oxon OX14 3DB, UK*
[6]*MIT Plasma Science and Fusion Center, 175 Albany St., Cambridge, MA 02139, United States*
[7]*Princeton Plasma Physics Laboratory, PO Box 451, Princeton, NJ 08543, USA*
[8]*General Atomics, PO Box 85608, San Diego, CA 92186-5608, USA*
[9]*Oak Ridge National Laboratory, Oak Ridge, TN 37831, USA*
[10]*Japan Atomic Energy Agency, Naka Fusion Institute, Naka, Ibaraki 311-0193, Japan*

Email: e.wolfrum@ipp.mpg.de
* See http://www.euro-fusionscipub.org/mst1

Abstract

Plasmas in machines with all metal plasma facing components have a lower Z_{eff}, less radiation cooling in the scrape-off layer and divertor regions and are prone to impurity accumulation in the core. Higher gas puff and the seeding of low-Z impurities are applied to prevent impurity accumulation, to increase the frequency of edge localised modes and to cool the divertor. A lower power threshold for the transition from low-confinement mode to high confinement mode has been found in all metal wall machines when compared to carbon wall machines. The application of lithium before or during discharges can lead to ELM free H-modes. The seeding of high-Z impurities increases core radiation, reduces the power flux across the separatrix and, if applied in the right amount, does not lead to deterioration of the confinement. All these effects have in common that they can often be explained by the shape or position of the density profile. Not only the peakedness of the density profile in the core but also the position of the edge pressure gradient influences global confinement. It is shown how i) ionisation in the pedestal region due to higher reflection of deuterium from high-Z walls, ii) reduced recycling in consequence of lithium wall conditioning, iii) the fostering of edge modes with lithium dropping, iv) increased gas puff and v) the cooling of the scrape-off layer by medium-Z impurities such as nitrogen affect the edge density profile. The consequence is a shift in the pressure profile relative to the separatrix, leading to improved pedestal stability of H-mode plasmas when the direction is inwards.

1. Introduction

The high erosion rates of carbon as well as the large co-deposition of hydrogen isotopes on carbon plasma facing components (PFCs) [1] has led to the decision to change to metal PFCs in several machines. While Alcator C-Mod has been operated with a molybdenum wall since 1993 [2], ASDEX Upgrade gradually changed from a carbon first wall to a fully tungsten

coated first wall from 1999 until 2007 [3], and JET has implemented the so-called ITER-like wall (ILW) in the year 2011 [4], consisting of beryllium coated main chamber plasma facing components (PFCs) and W divertor tiles.

With the change from carbon PFCs to metal ones, both ASDEX Upgrade (full W) and JET (Be, W) experienced some changes of plasma behaviour, such as a lower power threshold at the transition from L-mode (low-confinement mode) to H-mode (high-confinement mode) [5, 6] and the difficulty of running well heated discharges at low density [7, 8, 9, 10]. The transition to a full metal wall has removed carbon as main radiator in the scrape-off layer (SOL) and the divertor region, consequently leading to higher divertor temperatures [11]. With C missing as SOL radiator, W is sputtered in the hot divertor and can accumulate in the core. Not only the change to a full metal wall, but also the predicted heat loads for ITER [12, 13] call for additional divertor cooling, which is realised by puffing D and by seeding of impurities. Experiments with impurity seeding have been carried out on machines worldwide, e.g. C-Mod, JET, EAST, D-IIID, JT60-U and AUG with different effects on plasma confinement. While seeding nitrogen in machines with carbon PFCs did not have any positive effect on confinement [14], it can replace carbon as radiator in the SOL and the divertor in metal-clad machines and can sometimes lead to improved confinement [15, 16]. Experimentally, not only N results in improved confinement, also the seeding of lithium improves the plasma performance, as has been demonstrated in NSTX [17], EAST [18] and DIII-D [19]. In NSTX it is a consequence of reduced recycling, while in DIII-D a mode in the pedestal is fostered which increases particle transport across the edge transport barrier.

High radiation scenarios with a significant fraction of radiation in the core plasma as well as in the divertor are investigated in Alcator C-Mod, JT60-U and ASDEX Upgrade in order to reduce the power across the separatrix.

In all these experiments a common observation is that the pedestal properties are changed. Some influence the temperature directly by higher local radiation, others change the position of the density profile, which in turn alters the pedestal stability. In addition to pedestal structure changes, the ELM behaviour is also altered, presenting a new view of the ELM as a combination of a fast magneto hydrodynamic (MHD) crash and a subsequent slower transport event.

Far from being complete, in this review we will show in which way the metal wall changes the pedestal properties, why seeding impurities can improve confinement and how high radiation scenarios affect the pedestal and the core.

Because the leading theory which describes the limits to the pedestal pressure is the peeling ballooning theory, in section 2 a brief sketch is presented of how the pedestal stability reacts to changes in the pressure profile position and in the core normalised pressure. The actuators which change the pressure profile are described. Section 3 describes the effect of particle and energy reflection of D from C- and W-walls on the density profile with its consequence on both the power threshold for the transition from L- to H-mode and the change of plasma performance in AUG and JET with all metal PFCs. In section 4 wall conditioning and lithium seeding experiments are summarised, again with an emphasis on the achieved changes due to the location of the pedestal density profile. The effects of N seeding as well as effects of increased fuelling are reported in section 5 and finally, in section 6 the results of highly radiative scenarios with medium- to high-Z core radiation experiments as well as combined core and edge radiators are presented.

2. Pedestal stability reaction to pressure profile location and core pressure as well as actuators

Pedestal stability is calculated from linear ideal MHD theory where a dominant role is played by the magnitudes of the edge pressure gradient and the edge current density and its gradient. The strong edge pressure gradients drive ballooning modes on the outboard mid-plane while the concomitant large edge current density peaks drive kink/peeling modes, both of which then couple to peeling-ballooning modes [20, 21].

A standard stability diagram depicts the mode number with maximum growth rate of such modes in dependence of the normalised pressure gradients α (with $\alpha = -2V'/(4\pi^2)\cdot(V/(2\pi^2 R_0))^{1/2}\mu_0 p'$, with V being the plasma volume, R_0 the major radius, μ_0 the vacuum permeability, p the pressure and the prime denotes the derivative with respect to the poloidal flux ψ [22]) and peak edge current densities j. However, the parameters α and j are not the only factors influencing the pedestal stability; the plasma shape, the pedestal width, the core pressure and the relative position of the pressure gradient to the calculation boundary, which is equivalent to the separatrix in experiments, are also important. Plasmas with higher shaping can sustain higher α-values, while wider pedestals lead to a flattening of the sustainable α as more m-modes can become unstable. An increased core pressure changes the Shafranov shift and consequently the edge q profile and thereby stabilises ballooning modes, again allowing higher α. The further inside the plasma α_{max} is located, the lower j and

j' is at the separatrix reducing the drive for kink/peeling modes, also leading to higher α. Conversely, localising the edge pressure gradient further towards the separatrix flattens the q profile and the smaller q shear has a destabilising effect on high n modes [23, 19].
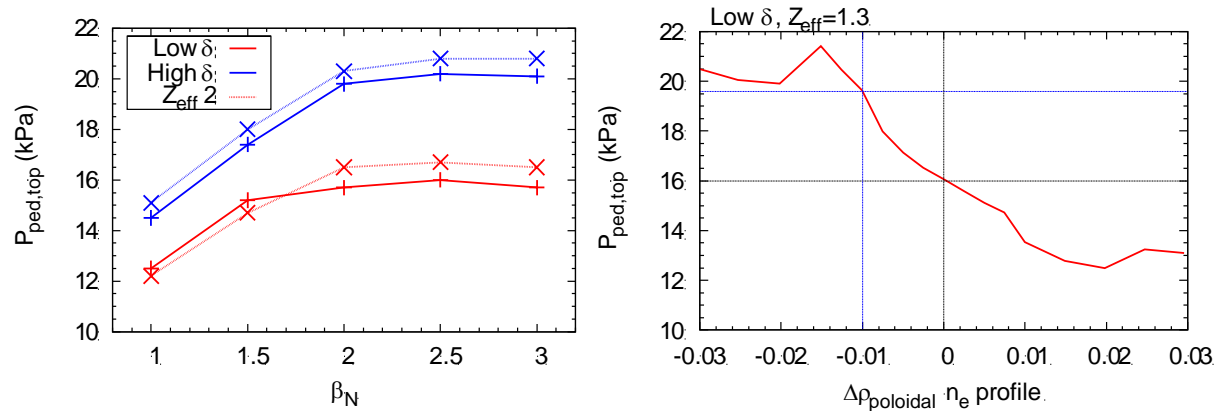

Figure 1: Linearly stable maximum pedestal top pressure a) vs. normalised total β for high and low shaping and $Z_{eff} =1.3$ (solid lines) and $Z_{eff}=2$ (dashed lines) and b) vs. the position of the n_e profile with fixed T_e profile position. An inward shift of $\rho_{pol} = -0.01$ (indicated in blue) with respect to the reference position (indicated in black) leads to an increase of $P_{ped,top}$ by 25%. Calculated for AUG equilibria.

Figure 1a shows how the maximum achievable pedestal top pressure calculated with a predictive stability work flow [24] using the ideal MHD stability code MISHKA [25] for a low and a high triangularity (δ) equilibrium depends on the total pressure, expressed as β_N. Also shown is the small effect of an increased effective charge $Z_{eff} = 2$ (dashed lines) over the reference $Z_{eff} = 1.3$ (solid lines). An increase in β_N from 1.5 to 2.5 leads to increased pedestal top pressure values by 5-10 % for low-δ plasmas and ~15% for high-δ plasmas in typical ASDEX Upgrade plasmas. In Figure 1b the effect of the position of the pressure profile is demonstrated. A small shift of only 5 mm (here equivalent to $\Delta\rho_{pol} \sim 0.01$) further inside and away from the boundary leads to an improvement of the stable pedestal pressure by 25%. Together these two effects can lead to a self-amplifying loop: if the pressure profile is shifted further inside, higher pedestal pressures can be achieved and yield higher core pressures via stiff temperature profiles, which in turn allow even higher pedestal top pressures.

2.1 Actuators which influence the pressure profile in the pedestal

The pressure profile is composed of the temperature and the density profile. It has been shown that the boundary condition of the electron temperature profile at the separatrix can be

described by the two-point model [26], in which collisional heat conductivity along the field lines connects the mid-plane with the divertor target plates. The strong dependence of heat conductivity on the temperature as well as the increase of heat flux with the parallel temperature gradient does not allow large changes of the separatrix electron temperature at similar heating powers. A lowering of the separatrix temperature could be expressed as a shift of the pressure profile inward [27] with the same effect on pedestal stability as a shift in the electron density (n_e) profile depicted in figure 1b. A significant shift of the electron temperature (T_e) profile can only be achieved with a dramatic reduction of heat flux across the separatrix. Because the density profile is governed by a complex interplay of poloidally varying transport and ionisation sources, the edge density profile position is much more flexible than the position of the electron temperature profile.

With these effects on the behaviour of the pedestal stability in mind, the actuators which influence the position of the density profile in the pedestal will now be discussed with special attention to wall materials and impurity seeding.

2.1.1 Wall materials

Due to the larger mass and charge difference the particle and energy reflection coefficients from high-Z PFCs are increased in comparison to low-Z PFCs, leading to more neutral particles with a larger mean free path [28]. Already early experiments on TEXTOR with a twin test limiter [29], one made from C and one from W, showed experimentally a much higher velocity distribution of recycled D from the W limiter. The faster D neutrals can penetrate further inside the separatrix, where they form a local ionisation source and contribute to the pedestal density and its gradient.

2.1.2 Recycling changes

The reduced fuel retention for metal walls has been confirmed experimentally [7]. Other methods such as boronisation [30, 31], siliconisation [32] and recently the application of lithium (see section 4) before a plasma discharge change the pumping efficiency of PFCs. The result is a reduction of the recycled particle flux and consequently a reduction of ionisation, which is a source to the density profile in the SOL and the pedestal. Also, if only the density value at the separatrix is reduced with otherwise self-similar profile shapes, this leads to a radial inward shift of the total pedestal pressure gradient.

2.1.3 The high field side high density region

It has been found that a SOL-zone of high density on the high field side at the height of the x-point called the high field side high density region (HFSHD) [33] plays a crucial role, as it influences the value of the separatrix density while the region itself can be influenced by the heat flux into the SOL. Indications of the existence of the HFSHD region at JET were already reported in 2009 [34]. To trigger the HFSHD region the inner divertor has to be detached and the heating power has to be sufficiently high. The HFSHD region can be reproduced in SOLPS simulations, in which the combination of drifts and an additional convective transport are introduced. The HFSHD region leads to inverted radial n_e profiles outside the separatrix and consequently to core fuelling due to diffusion [35]. Impurities such as C or N are strong radiators in the SOL, and thus lead to a cooling of the electron temperature in the SOL and consequently reduce the ionisation rate in this area. A reduction of the density in the HFSHD region comes with a reduction in $n_{e,sep}$ and a shift of the pressure profile inward, away from the separatrix.

2.1.4 Modes in the pedestal region

Electrostatic or electromagnetic highly localised modes can appear in the pedestal and can modify the shape of the density profile, effectively shifting α_{max} further inward, away from the separatrix.

3. Observations of changes to the pedestal after the changeover to all metal PFCs at AUG and JET.

With the change from a machine with C PFCs to a fully clad metal machine it was possible to make direct comparisons of the effect of the first wall material on the pedestal and confinement in an otherwise unchanged machine. Some observations are similar in AUG and JET, but others are different. In both it was found that the operational space with no gas puff, which used to yield discharges with the best performance in all-C machines, is very limited, due to the accumulation of high-Z impurities in the core [36]. In both machines, the pedestal top temperature values in particular were considerably lower, the effect propagating towards the core via stiff core temperature gradient lengths.

In AUG no difference in performance was found when stable discharge phases without gas puff were compared. This means that in AUG the expected pedestal top pressure was measured for both wall materials, albeit at lower pedestal top temperatures [37]. In JET however, different effects were observed with high and low-triangularity discharges. Figure 2 shows the achieved pedestal top densities and temperatures for both high- and low-triangular discharges in comparison with the values achieved for highly shaped plasmas in the all C machine (grey) [38 and references therein].
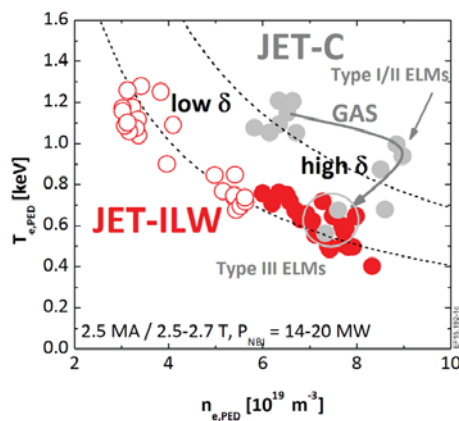

Figure 2: taken from reference [38]. Comparison of pedestal top electron temperature vs. electron density for low- and high-triangularity discharges in JET-ILW to JET-C. The ILW cases lie consistently on a lower pedestal pressure curve.

In the JET-ILW cases the increased pressure usually achieved in high-triangularity discharges in JET-C cannot be observed [39], but plasmas with both shapings lie on the same pressure curve [8, 38]. In contrast to the low-triangularity discharges the ones with high shaping are not consistent with peeling-ballooning stability. A low D puff was found to be necessary for good confinement in JET with the ILW and higher gas puff rates reduced confinement, at the same time resulting in wider pedestals [38]. This was found to be not consistent with the ideal peeling-ballooning predictions and it was concluded that recycling or a Z-dependence of impurities changes the peeling ballooning conditions.

In AUG, however, lower pedestal top temperatures but very similar pedestal pressure profiles were observed even without significant core radiation. In Figure 3 the pedestal profiles of discharges in AUG with two different heating powers (8 and 13 MW) once in C PFCs (black) and once with full W PFCs (red) are shown [37], all phases are without gas puffing. It can be seen that the pedestal pressure profiles (c,f) are similar, the composition however is changed towards higher densities and lower temperatures.
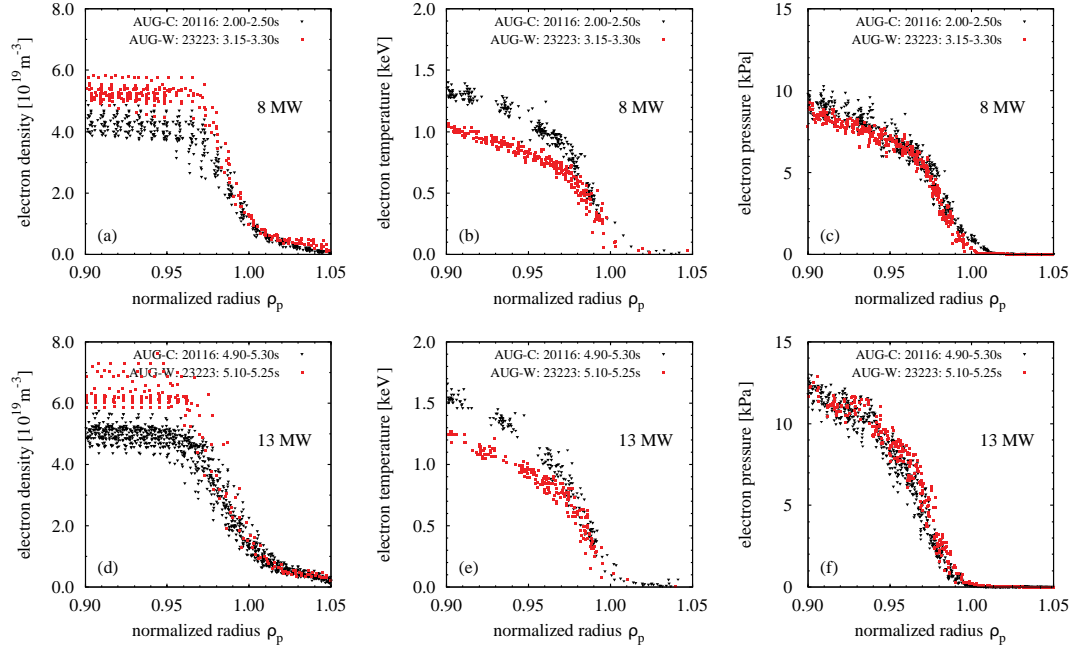
Figure 3: AUG data taken from reference [37]. Edge electron density (a,d), temperature (b,e) and pressure profiles (c,f) for 8 and 13 MW discharges without gas puff in AUG. Black profiles are with C PFCs and red ones with W PFCs.

An explanation for this behaviour can be found in the increased particle and energy reflection of D from high-Z wall materials when compared to C PFCs. The longer mean free paths of the reflected neutral D atoms lead to an increased fuelling. Taking into account the different reflection properties of the PFCs, modelling with EMC3-Eirene has shown that the fuelling is mainly caused by the divertor neutrals under low density conditions [40]. The increased ionisation source in the pedestal region results in higher densities and consequently in lower temperatures under otherwise similar conditions, such as no gas puff and same heating power. For higher densities, however, the impact of the wall material on the profiles is reduced, because the ion temperature, and therefore the energy of the neutrals at the target become smaller and the SOL more opaque to neutral penetration.

At AUG this same effect could also explain the lower L-H power threshold, as the same critical radial electric field shear could be achieved with less heating power, because the increased density gradient length compensates part of the necessary heating power [41]. The lower L-H power threshold also found at JET [6] was attributed to a change in Z_{eff}.

At the EAST tokamak, which is equipped with a Mo wall and graphite divertors, a lower L-H power threshold was measured with the metal first wall as compared to the all C machine. While the lowest power threshold and best confinement was achieved in double null configuration, there is an oddly low power threshold when operating in the unfavourable ion-

∇B direction, and a higher than expected power threshold in the lower single null configuration which was speculatively attributed to an effect of Li wall conditioning only applied in the LSN discharge [42].

In summary, metal walls can lead to a higher particle and energy reflection of recycled neutrals. Not only more D atoms are reflected from high-Z PFCs but they also carry a higher velocity, penetrating further inside the confined region. This causes the observed increase in density in discharges without gas puff and also the reduced L-H power threshold at AUG. The observed oddly high L-H power threshold in the EAST tokamak in the usually favourable configuration may also be explained by the fact that only in this case Li wall conditioning was applied and led to reduced recycling as well as to lower particle reflection.

The observations at JET cannot be explained yet. It is still an open question as to why the high-triangularity discharges do not reach pedestal top values as expected from peeling-ballooning stability calculations.

4. Wall conditioning and Li seeding

Wall conditioning by boronisation or siliconisation is used on several tokamaks in order to reduce the oxygen content in the vessel. Experimentalists at the NSTX tokamak were the first to also apply lithium before discharges in order to condition the walls. Lithium acts as a pump, thus reducing recycling. The characterisation of the pedestal in Li pre-conditioned discharges showed that the more Li is used the more the density profiles are shifted further inwards, until the discharge even becomes ELM free [43, 44, 45].

With thick lithium coatings, the plasma reached a global stability limit while the edge remained stable to ELMs. It was shown that if the pressure profile is located further away from separatrix edge stability is improved [46]. The effect of lithium is mainly a reduction of recycling by ~10%, leading to a wider zone of reduced transport [47]. The authors conclude that 'These results suggest that lithium, and wall conditioning and pumping techniques in general, may be a strong lever in controlling the properties of the H-mode pedestal.'[48].

A subsequent analysis of micro-instabilities showed that electron temperature gradient modes (ETG) can be found in both cases, in accordance with the fact that the T_e gradient lengths do not change, micro tearing modes (MTMs) at the pedestal top become stabilised as steep n_e profiles become wider, and that micro-instabilities become trapped-electron mode (TEM) like

with growth rates of the same order as ExB shearing rates. The role of kinetic ballooning modes (KBM) remains unclear [49]. Figure 4 shows the edge profiles of highly shaped plasmas in NSTX with different amounts of lithium evaporated before the discharge [50].
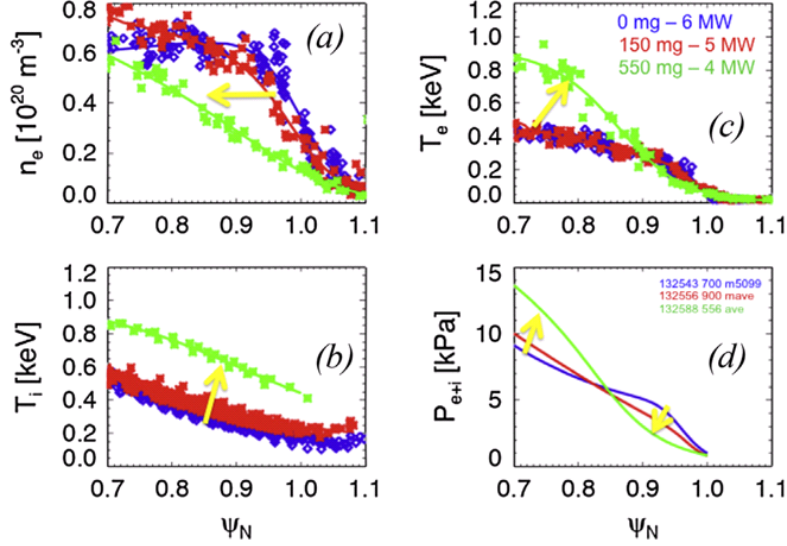

Figure 4: NSTX data taken from reference [50]. Comparison of edge profiles for three discharges with different levels of pre-discharge lithium evaporation. Arrows indicate the direction of increasing pre-discharge lithium. Note that there is a difference in NBI heating power also.

The edge density profile is clearly shifted further inward with increasing levels of pre-discharge lithium evaporation (a), allowing a higher pedestal top pressure (d). At the same time the mid-plane neutral pressure was found to be reduced.

At the EAST tokamak, a study comparing boronisation, siliconisation and lithium vaporisation before and during pulses showed that the hydrogen content could only be reduced significantly using lithium. The lithium vaporisation led to H-mode plasmas in EAST [51]. With application of Li long 30 s H-modes could be performed with small ELMs and a quasi-coherent mode (QCM) with frequencies around 30-50 kHz [18]. Two different enhanced recycling regimes have been identified, both showing QCMs which increase transport across the separatrix. While the low enhanced recycling regime is unstable with increased radiation and a density rise occurs, in the high enhanced recycling regime the QCMs provide enough transport to remain stable [52]. The edge coherent mode (ECM) established in EAST discharges with real-time lithium aerosol injection provides energy and particle transport so that an ELM-free phase is achieved and maintained for 18 s [53, 54].

Also at DIII-D the application of lithium aerosoles, which were dropped in the vessel during the discharges led to a change of the edge density profile shape. A so-called 'bursty chirping mode' (BCM) was found to flatten the density profile, effectively leading to a shift of the pressure profile further inward, away from the separatrix. This effect can clearly be seen in Figure 5a-c), where only the red n_e profiles are modified by the BCM and subsequently allow higher pedestal top pressures.
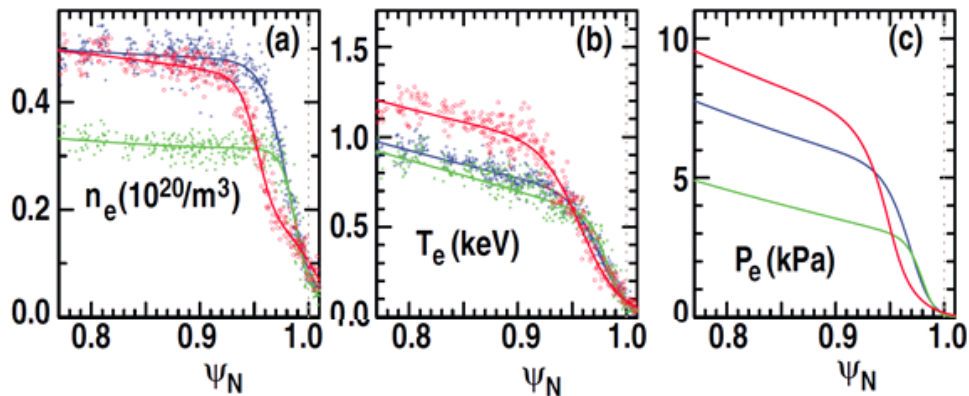

Figure 5: DIII-D data, graph modified from reference [19]. Experimental profiles just before an ELM (red) near the end of a 225 ms ELM-free period with BCM, (blue) near the end of a 290 ms ELM-free period without BCM and (green) near the end of a 20 ms ELM-free period without BCM.

In the same work, it was shown that the shift of the pressure profile leads to a change of the ideal peeling-ballooning stability boundary, as depicted in
Figure 6 for the experimental conditions shown in Figure 5. Clearly the inward shift of the pressure gradient results in the higher achievable normalised pressure gradient α [19]. In summary, the application of lithium leads to either reduced recycling or to the appearance of edge modes, both effects influencing the edge density profile and consequently the position of the pressure profile with respect to the separatrix.
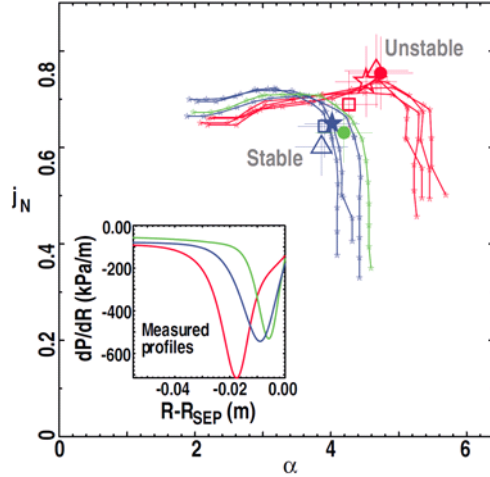
Figure 6: DIII-D, taken from reference [19]. Comparison of experimental data just before an ELM to PBM stability threshold computed with the ELITE code as a function of peak normalised pressure gradient in the pedestal region, α, and normalised pedestal current density, j_N, with $j_N = (j_{PB} + j_{PB}^{SEP})/(2I_P A)$ and $j_{PB}^{(SEP)}$ is the flux surface averaged current density (at the separatrix), I_P the plasma current and A the flux surface area. Colours are the same as in Figure 5.

5. Gas puffing, N and C seeding

The absence of carbon as a divertor radiator leads to increased divertor temperatures. As the sputtering is a function of temperature as well as low Z impurity concentration with a maximum at medium concentration levels, situations with higher sputtering can occur and consequently lead to an increase of high-Z impurities. At the same time, the edge density profiles are steeper due to the increased energy and particle reflection (see section 3), so that the neoclassical inward impurity transport is stronger, giving rise to situations in which impurity accumulation in the core leads to radiation collapse of the discharges.

One of the measures to prevent core impurity accumulation is to apply an increased gas puff, which firstly increases the ELM frequency, thus transporting high-Z impurities out of the confined zone again [55], and secondly cools the SOL and divertor by a rise of density and radiation, thus reducing the sputtering. Just as in C machines the increased fuelling leads to confinement loss of the order of 10-20% [56, 36, 15, 57].

In AUG experiments with the aim of taking the discharge up to the density limit [58] a strong gas puff combined with reduced pumping speed leads to a rise of neutral pressure in the divertor. The corresponding edge electron density and temperature profiles are shown in Figure 7. Phase 1 is still a stable H-mode with good confinement. H-mode confinement

deteriorates and a transition to type-III ELMs occurs during phase 2, as well as the development of a density shoulder in the SOL. In phase 3 the H-mode breaks down until it falls back into L-mode (phase 4). Figure 7 demonstrates that the rising fuelling causes a rise of the density at the separatrix, shifting the pedestal n_e profiles to higher values without a change in gradient. Together with an almost fixed separatrix electron temperature, this leads to an outward shift of the electron pressure profile and hence to a degradation of the H-mode pedestal pressure.
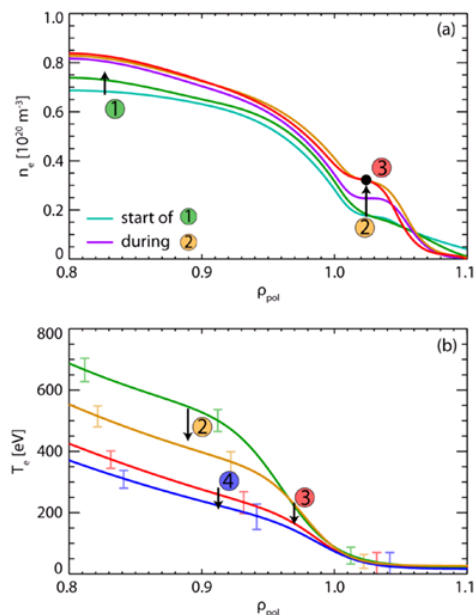

Figure 7: AUG data taken from reference [58]. Development of edge electron density and temperature profiles for increased neutral pressures. Phase 1 is a stable H-mode, phase 2 a deteriorating H-mode, in phase 3 the H-mode breaks down and transits back to L-mode (phase 4).

As already described in section 2.1.3, under high recycling conditions a region of high density exists in the HFS SOL at the height of the x-point, called high field side high density (HFSHD) region [33]. Apart from high recycling sufficient heating power is required for its build-up with densities up to 10 times larger than the separatrix density. In this region inverted n_e profiles cause diffusive transport towards the confined region [35]. When N is seeded, the SOL is cooled via radiation, the HFSHD decreases, $n_{e,sep}$ is reduced and the edge pressure profile position moves again further away from the separatrix, with the previously described effect on linear MHD stability.

With dedicated CD_4 seeding experiments it was demonstrated that C has the same effect as N, in that it reduces the density in the HFSHD region [59]. On the other hand, seeding of N in a C machine did not show any beneficial effects on pedestal stability [14, 57]. In a comparison

of JET and AUG with all metal walls it was shown that the operation with gas puff deteriorates confinement, but N seeding causes confinement improvement in both machines [36].

The experimental findings at JET can be summarised as follows: The ILW leads to lower pedestal top temperatures and lower confinement than equivalent discharges with a C wall [60, 39]. In a JET C/ILW comparison of discharges at high δ a lower pedestal temperature leading to 30% less confinement was found in the ILW case, with the relation H_{98}-$p_{e,ped}$ retained in both cases. Stable high δ discharges, with $H_{98,y2} \sim 0.85$ and low ELM losses were achieved for 7 s, which is equivalent to 28 confinement times [61]. With N seeding the pedestal top temperature increased, partially recovering the confinement losses [39]. An analysis of the pedestal structure of discharges with horizontal target revealed that with application of N seeding the pedestal, and especially the temperature profile, widens [62]. Taking into account these effects of a widened edge profile as well as the increased core pressure in the edge stability analysis in JET, agreement with peeling-ballooning stability can be achieved by shifting the pedestal inward. The increased Shafranov shift, higher edge current and wider pedestal results in better confinement. In this analysis the artificial shift is achieved via a reduction of $T_{e,sep}$ from 100 to 80 eV [27]. The recovery of confinement with seeding is not observed at low δ discharges at JET. An explanation for the different responses of JET and AUG discharges to the seeding of nitrogen might be that the operational points are found in different positions in the peeling ballooning diagram: while AUG discharges can be located in the PB corner, the JET discharges sit more at the ballooning boundary and as a result the same explanation does not have to apply. It is likely that more than one mechanism is at play here [61].

At AUG it was found that the improvement of N seeding stems mainly from the pedestal with only a small contribution from core density peaking [24]. An orthogonal effect of shaping and seeding was determined: while shaping mainly increases the pedestal density, seeding increases the temperature. Also the ELM behaviour is changed with N seeding. Both at JET [63] and AUG [64, 65] it is found that the ELM frequency is increased, with a shortened ELM length and a concomitant reduction in the individual ELM loss. While the first phases of both, long and short ELMs, are very similar, the long ELMs have a subsequent phase of increased transport, which is missing completely in the short ELMs. The total losses due to ELMs are not changed.

Figure 8 shows the development of ELMs with an increasing N puff. Although the pedestal top temperature increases, the number of long ELMs, N_{long}, becomes smaller and the short ELMs, depicted in orange in fig 8c, become more frequent. At the end of the N puff, the short ELMs cause about the same energy loss, ΔW_{ELM}, as the long ELMs at the beginning of the N

puff. As the initial phase in the long ELMs is the same as in the short ELMs, the peak power losses of both, long and short ELMs, are the same, so that neither one is more beneficial in terms of divertor power load.

A more detailed analysis revealed that also in discharges without N seeding long and short ELMs can be observed. It seems that the disappearance of long ELMs is related to a reduction of the SOL or divertor temperature; the exact mechanism, however, is not yet clear. In summary, the experimental observations may consistently be explained by the effect which the edge pressure profile position has on the edge stability: increasing the D gas puff leads to a rise of the separatrix density shifting the pressure profile outward and puffing N reduces the HFSHD region and consequently the separatrix density, allowing the recovery of confinement. Additionally, there seems to be a connection between a cooled SOL or divertor and the disappearance of the second phase observed in long ELMs.
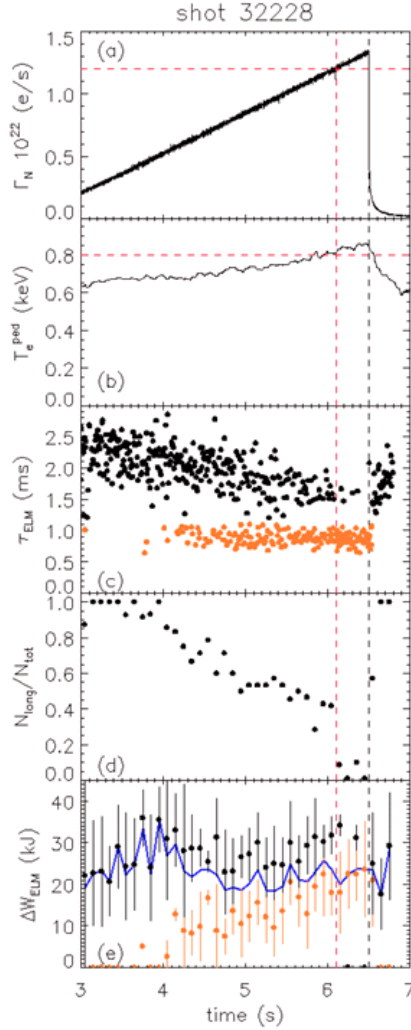
Figure 8: AUG data taken from reference [65]. Time evolution of (a) nitrogen puff rate, (b) pedestal temperature, (c) ELM duration, (d) N_{long}/N_{tot}, and (e) ELM energy losses for AUG discharge #32228 (P_{NBI}=10MW). In frames (c) and (e), long ELMs are in black and short ELMs in orange. The red vertical line highlights the time at which N_{long}/N_{tot} drops. The vertical black line highlights the time at which nitrogen flow is tuned off. The blue line in frame (e) highlights the energy losses calculated without separating long and short ELMs.

6. Medium- and high-Z radiation

In order to meet the material limits in future reactors the power flux to the divertor target plates needs to be reduced. For this purpose, plasma scenarios with high radiated power fractions are required. While for ITER most of the exhaust power can be dissipated in the SOL, for DEMO radiation losses in the confined region are required to decrease the power across the separatrix. The application of low- and medium-Z impurities such as N and Ne

16

increases primarily the SOL radiation. High-Z impurities such as Ar, Kr or W radiate mostly in the core.

To retain the enhanced energy confinement of the H-mode, the power flux across the separatrix has to stay above the H-L threshold. Therefore, at ITER additional radiation in the core is not feasible, but for DEMO the expected excess of α-heating above the H-mode threshold allows (and requires) significant core radiation.

At AUG the seeding of N leads to reduced or increased sputtering depending on divertor plasma temperatures and to improved confinement as has been shown in the previous section. High ELM frequencies are achieved with N seeding, in contrast to Ar seeding which reduces the ELM frequency and in case of too much Ar seeding leads to peaked density profiles and impurity accumulation [66].

At JT-60U better confinement with Ar seeding is achieved, accompanied by peaked core density profiles, as well. The dilution in the pedestal allows higher pedestal temperatures [67]. Ar seeding also reduces the ELM frequency, as is shown in Figure 9a), which is not so much an effect of the density (Figure 9b), but a direct consequence of the power crossing the separatrix being reduced by radiation in the confined region (Figure 9c).
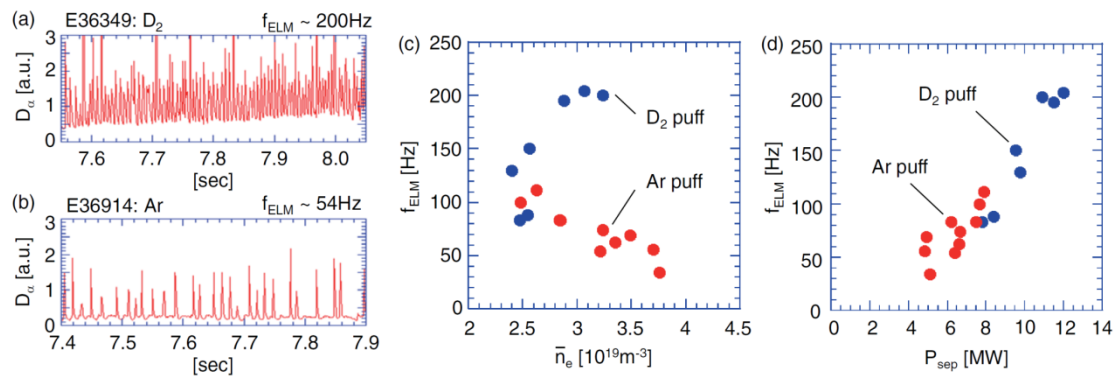

Figure 9: JT60-U data taken from reference [67]. The D_α emission rate from the outer divertor region for the cases of (a) deuterium puff and (b) argon puff at a given Greenwald density fraction of 0.56. (c) f_{ELM} as a function of averaged n_e. (d) f_{ELM} as a function of the power across the separatrix P_{sep}.

A comparison of N and Kr as radiators at AUG showed that N radiates near the x-point and inside the x-point, while Kr produces a radiative ring inside the separatrix at the top of the pedestal [68]. This combination was successfully used in double radiation feedback experiments applying both N and Kr as radiators. It was shown that core losses are induced by Ar or Kr, while N radiates mainly in the divertor [69]. The seeding of only N allowed

complete detachment to be achieved with the occurrence of benign type-III ELMs in 1.2 MA plasmas at AUG [70].

Also at Alcator C-Mod moderate impurity seeding of N, Ne and Ar results in a considerable improvement of plasma confinement, which is also related to an increase of the temperature at the pedestal top, concomitant with an inward shift and a widening of the pressure profile [71]. Stronger N, Ne and Ar seeding experiments could keep good confinement with 85% radiation, with the power across the separatrix only marginally above the L-H power threshold. At the same time the divertor heat flux could be reduced by a factor 5 [72].

In JET with C PFCs a fuelling study was carried out to drive the divertor into detachment. N and Ne seeding was applied with a maximum radiated power fraction of 55% in stable H-modes with type-I ELMs. At higher values the transition to type III ELMs was observed [57]. Investigations of N and Ne seeding in the JET ILW also demonstrated good confinement and reduced exhaust with partially detached divertors [73].

In summary the core radiators can act via two effects on the pedestal: firstly, dilution due to the high charge of the medium- to high-Z impurities yield a lower total pedestal top density, allowing a higher pedestal top temperature to reach the same stability limit. These discharges have lower core collisionality resulting in a more peaked density profile and secondly, radiation in the confined region, which lowers the heat flux across the separatrix. The consequent slow build-up of the pedestal top can reduce the ELM frequency strongly, sometimes causing an increase of impurity accumulation because the flushing out by ELMs is diminished.

7. Summary and conclusions

When deuterium ions impinge on PFCs, they are neutralised and can be reflected from the wall, re-entering the plasma as neutrals. The particle reflection coefficients as well as the energy reflection coefficients from W-PFCs are both considerably larger than from C-PFCs. Consequently, with W-PFCs the neutral flux across the separatrix is larger in case of a thin, transparent scrape-off layer (SOL) and leads to better fuelling of the core plasma. In L-mode this effect causes steeper edge density gradients in ASDEX Upgrade, thereby contributing more to the critical flow shear assumed to be necessary for the L-H transition. The same effect could explain the observations of a lower L-H power threshold in EAST in a high-Z PFC machine. Also the observed increased power threshold in favourable configuration after

the application of lithium wall conditioning might be explained by the contrary effect, namely the flattening of the edge density profile due to reduced recycling.

Also at JET a reduced L-H power threshold is observed, which is currently attributed to the lowering of Z_{eff} in the all metal wall.

The conditioning of the vessel with lithium before a discharge in NSTX has shown to improve the pedestal performance, and the dropping of lithium during a discharge in DIII-D has led to ELM free phases with high confinement. In both cases stability analysis shows that the inward shift of the density profile caused by either reduced recycling or a mode in the pedestal region is the reason for improved stability and consequently higher pedestal top pressures.

In H-modes without gas puff the effect of higher reflection from high-Z walls can lead to higher pedestal top densities. With the pedestal pressure profile being limited by ELMs otherwise same discharge parameters result in lower pedestal top temperatures but the same critical edge pressure profiles as shown in AUG. If, however, the reduction of the edge temperature is stronger than the increase of the density, a reduced total pressure is the consequence. The effect of reduced β_N on the edge stability is detrimental and only a lower critical edge pressure gradient can be achieved.

In metal walled machines there is no intrinsic SOL radiator. This leads to higher target temperatures and to increased sputtering in the hot SOL. In order to cool the divertor and the SOL either D puffing or seeding of low-Z impurities such as nitrogen (N) can be applied. When applying D gas puffing and with sufficient heat flux across the separatrix, a high density region at the HFS at the height of the x-point is created, forming an inverted density profile which, via diffusion, increases the separatrix density. This raise of the density profile causes an outward shift of the edge pressure profile and thus a reduction of the edge stability. The loss of stability can be regained by N seeding, because radiation cooling reduces the available energy in the SOL and consequently also reduces the density in the HFSHD region. At AUG at high densities N seeding has been shown to shift the edge density profile further in w.r.t. the edge electron temperature profile, resulting in an edge pressure profile further inward from the separatrix, and due to improved MHD stability, in a higher critical pedestal top pressure. At JET a tentative alternative explanation, involving the reduction of the separatrix temperature, but leading to an inward shift of the edge pressure profile with a consequently higher critical pedestal top pressure as well, was proposed. The self-amplifying loop of increased pedestal top temperatures – stiff temperature profiles – higher core β – shift

of stability boundary towards higher pressure gradients can explain why N seeding in machines with metal PFCs allows the recovery of plasma parameters at high fuelling rate and ELM frequency.

In discharges with N seeding a change of ELM behaviour is observed, where without N seeding long ELMs, up to 4 ms duration, were replaced by short ELMs (< 1 ms) when N was seeded. The same effect can be observed with D puffing only, so it is not an effect of Z_{eff} or the impurity itself. The reduced ELM length occurs together with an increased ELM frequency so that the total ELM loss power is hardly changed. Also the peak heat loads are not reduced in plasmas with short ELMs as the first phase of the long ELM is very similar to a short ELM.

A combination of medium- and high-Z impurities seeding together with high fuelling can be used to build a suitable radiation profile for main chamber as well as divertor radiation, in order to avoid localised overheating of the divertor. A radiative layer just inside the separatrix does not necessarily deteriorate confinement. The dilution by high-Z impurities can result in a lower total density allowing a higher pedestal top temperature, which in combination with a peaked core density profile yields improved confinement.

In conclusion, this overview has shown that the density profile shape and position relative to the separatrix is influenced by the material of plasma facing components and can be modified by wall conditioning and seeding of various elements, namely lithium, CD_4, N, Ne, Ar and Kr. In order to be able to predict the performance of discharges in next generation devices the modelling of the exact density profile is indispensable. Necessary ingredients for such modelling are i) the quantitative prediction of the ionisation profile taking into account the 3D nature of the PFCs, ii) the particle transport across the pedestal in the inter-ELM phase due to modes in the pedestal region as well as due to the HFSHD region and iii) the particle losses due to ELMs.

In view of ITER it has already been recognised that the density dependence of the current confinement scaling [74] is not valid under certain conditions and that the scaling for the L-H power threshold [75] does not fit experimental results with all-metal walls. Both scalings are currently under revision.

Figure captions:

Figure 1: Linearly stable maximum pedestal top pressure a) vs. normalised total β for high and low shaping and $Z_{eff} = 1.3$ (solid lines) and $Z_{eff} = 2$ (dashed lines) and b) vs. the position of the n_e profile with fixed T_e profile position. An inward shift of $\rho_{pol} = -0.01$ (indicated in blue) with respect to the reference position (indicated in black) leads to an increase of $P_{ped,top}$ by 25%. Calculated for AUG equilibria.

Figure 2: taken from reference [38]. Comparison of pedestal top electron temperature vs. electron density for low- and high-triangularity discharges in JET-ILW to JET-C. The ILW cases lie consistently on a lower pedestal pressure curve.

Figure 3: AUG data taken from reference [37]. Edge electron density (a,d), temperature (b,e) and pressure profiles (c,f) for 8 and 13 MW discharges without gas puff in AUG. Black profiles are with C PFCs and red ones with W PFCs.

Figure 4: NSTX data taken from reference [50]. Comparison of edge profiles for three discharges with different levels of pre-discharge lithium evaporation. Arrows indicate the direction of increasing pre-discharge lithium. Note that there is a difference in NBI heating power also.

Figure 5: DIII-D data, graph modified from reference [19]. Experimental profiles just before an ELM (red) near the end of a 225 ms ELM-free period with BCM, (blue) near the end of a 290 ms ELM-free period without BCM and (green) near the end of a 20 ms ELM-free period without BCM.

Figure 6: DIII-D, taken from reference [19]. Comparison of experimental data just before an ELM to PBM stability threshold computed with the ELITE code as a function of peak normalised pressure gradient in the pedestal region, α, and normalised pedestal current density, j_N, with $j_N = (j_{PB} + j_{PB}^{SEP})/(2I_PA)$ and $j_{PB}^{(SEP)}$ is the flux surface averaged current density (at the separatrix), I_p the plasma current and A the flux surface area. Colours are the same as in Figure 5.

Figure 7: AUG data taken from reference [58]. Development of edge electron density and temperature profiles for increased neutral pressures. Phase 1 is a stable H-mode, phase 2 a

deteriorating H-mode, in phase 3 the H-mode breaks down and transits back to L-mode (phase 4).

Figure 8: AUG data taken from reference [65]. Time evolution of (a) nitrogen puff rate, (b) pedestal temperature, (c) ELM duration, (d) N_{long}/N_{tot}, and (e) ELM energy losses for AUG discharge #32228 (P_{NBI}=10MW). In frames (c) and (e), long ELMs are in black and short ELMs in orange. The red vertical line highlights the time at which N_{long}/N_{tot} drops. The vertical black line highlights the time at which nitrogen flow is tuned off. The blue line in frame (e) highlights the energy losses calculated without separating long and short ELMs.

Figure 9: JT60-U data taken from reference [67]. The D_α emission rate from the outer divertor region for the cases of (a) deuterium puff and (b) argon puff at a given Greenwald density fraction of 0.56. (c) f_{ELM} as a function of averaged n_e. (d) f_{ELM} as a function of the power across the separatrix P_{sep}.

References

[1]   R. Neu et al., Journal of Nuclear Materials 367–370 (2007) 1497–1502
[2]   I.H. Hutchinson et al., Physics of Plasmas 1 (1994) 1511
[3]   R. Neu et al., Plasma Phys. Control. Fusion 49 (2007) B59–B70
[4]   G. Matthews et al., Phys. Scr. T145 (2011) 014001 (6pp)
[5]   F. Ryter et al., Nucl. Fusion 53 (2013) 083023
[6]   C.F. Maggi et al., Nucl. Fusion 54 (2014) 023007 (15 pp)
[7]   R. Neu et al., Journal of Nuclear Materials 438 (2013) S34–S41
[8]   M. Beurskens et al., Nucl. Fusion 54 (2014) 043001 (13pp)
[9]   C.D. Challis et al., Nucl. Fusion 55 (2015) 053031 (18pp)
[10]   I. Nunes, Plasma Phys. Control. Fusion 58 (2016) 014034 (10pp)
[11]   M. Groth et al., Nucl. Fusion 53 (2013) 093016 (11pp)
[12]   R.A. Pitts et al., Journal of Nuclear Materials 438 (2013) S48–S56
[13]   R. Neu et al., Plasma Phys. Control. Fusion 53 (2011) 124040
[14]   A. Kallenbach et al., Plasma Phys. Control. Fusion 38 (1996) 2097–2112
[15]   J. Schweinzer et al., Nucl. Fusion 51 (2011) 113003 (7pp)
[16]   G. Matthews, Journal of Nuclear Materials 438 (2013) S2–S10
[17]   R. Maingi et al., Nucl. Fusion 52 (2012) 083001 (14pp)
[18]   J. Li et al., Nature Physics, Published online: 17 November 2013 | DOI: 10.1038/NPHYS2795
[19]   T. Osborne et al., Nucl. Fusion 55 (2015) 063018 (20pp)
[20]   J.W.Connor, Plasma Phys. Control. Fusion 40 (1998) 191-213
[21]   P.B. Snyder et al., Physics of Plasmas 5(9) (2002) 2037-2043
[22]   R.L. Miller et al., Physics of Plasmas 5 (4) (1998) 973-978
[23]   J. Loennroth et al., Nucl. Fusion 51 (2011) 013003 (9pp)
[24]   M. Dunne et al., submitted to PPCF
[25]   A.B. Mikhailovskii et al., Plasma Physics Reports 23 (1997) 844

[26] P. Stangeby 'The Plasma Boundary of Magnetic Fusion Devices' (Bristol and Philadelphia: Institute of Physics Publishing) 2000
[27] S. Saarelma et al., Physics of Plasmas 22 (2015) 056115
[28] W. Eckstein, IPP Report 17/12 (2009), IPP Garching
[29] A. Huber et al., Journal of Nuclear Materials 290-293 (2001) 276-280
[30] B. Lipschultz et al., Physics of Plasmas 13 (2006) 056117
[31] V. Rohde et al., Journal of Nuclear Materials 363–365 (2007) 1369–1374
[32] U. Samm et al., Journal of Nuclear Materials 220-222 (1995) 25.
[33] S. Potzel et al., Journal of Nuclear Materials 463 (2015) 541–545
[34] K. McCormick et al., Journal of Nuclear Materials 390-391 (2009) S465
[35] F. Reimold et al., this conference
[36] M. Beurskens et al., Plasma Phys. Control. Fusion 55 (2013) 124043 (13pp)
[37] P.A. Schneider et al., Plasma Phys. Control. Fusion 57 (2015) 014029 (12pp)
[38] C.F. Maggi et al., Nucl. Fusion 55 (2015) 113031 (15pp)
[39] C. Giroud et al., Nucl. Fusion 53 (2013) 113025 (12pp)
[40] T. Lunt to be submitted to PPCF
[41] L.M. Shao et al., Plasma Phys. Control. Fusion 58 (2016) 025004 (11pp)
[42] Z.X. Liu et al., Nucl. Fusion 53 (2013) 073041 (5pp)
[43] R. Maingi et al., Phys. Rev. Letters 103 (2009) 075001
[44] R. Maingi et al., Phys. Rev. Letters 107 (2011) 145004
[45] D.P. Boyle et al., Journal of Nuclear Materials 438 (2013) S979–S982
[46] D.P. Boyle et al., Plasma Phys. Control. Fusion 53 (2011) 105011 (15pp)
[47] J.M. Canik et al., Journal of Nuclear Materials 415 (2011) S409–S412
[48] J.M. Canik et al., Physics of Plasmas 18 (2011) 056118
[49] J.M. Canik et al., Nucl. Fusion 53 (2013) 113016 (11pp)
[50] R. Maingi et al., Journal of Nuclear Materials 463 (2015) 1134
[51] G. Z. Zuo et al., Plasma Phys. Control. Fusion 54 (2012) 015014 (10pp)
[52] H.Q. Wang et al., Nucl. Fusion 54 (2014) 124001 (12pp)
[53] J. S. Hu et al., Phys.Rev.Lett. 114, 055001 (2015)
[54] B. Wan et al., Nucl. Fusion 55 (2015) 104015 (20pp)
[55] R. Dux et al., Nuclear Fusion 51(5) (2011) 053002
[56] J. Hughes et al, Nucl. Fusion 47 (2007) 1057–1063
[57] C. Giroud et al., Nucl. Fusion 52 (2012) 063022 (22pp)
[58] M. Bernert et al., Plasma Phys. Control. Fusion 57 (2015) 014038 (12pp)
[59] M. Beurskens et al., Nucl. Fusion 56 (2016) 056014 (10pp)
[60] G.P. Maddison et al., Nucl. Fusion 54 (2014) 073016 (28pp)
[61] C. Giroud et al., Plasma Phys. Control. Fusion 57 (2015) 035004 (20pp)
[62] M. Leyland et al., Nucl. Fusion 55 (2015) 013019 (14pp)
[63] L. Frassinetti et al., Nucl. Fusion 55 (2015) 023007 (14pp)
[64] P.A. Schneider et al., Plasma Phys. Control. Fusion 56 (2014) 025011 (15pp)
[65] L. Frassinetti et al., submitted to NF
[66] R. Neu et al., Journal of Nuclear Materials 415 (2011) S322–S326
[67] H. Urano et al., Nucl. Fusion 55 (2015) 033010 (9pp)
[68] M. Bernert et al., EPS 2015
[69] A. Kallenbach et al., Plasma Phys. Control. Fusion 55 (2013) 124041 (10pp)
[70] A. Kallenbach et al., Nucl. Fusion 55 (2015) 053026 (8pp)
[71] J. Hughes et al., Nucl. Fusion 51 (2011) 083007 (8pp)
[72] A. Loarte et al., Physics of Plasmas 18 (2011) 056105

[73] G.P. Maddison et al., Nucl. Fusion 51 (2011) 042001
[74] ITER Physics Basis Nucl Fusion 39 (1999) 2175
[75] Y.R.Martin et al., J. Phys.: Conf. Ser. 123 (2008) 012033